Journal of Applied Fluid Mechanics, Vol. 16, No. 4, pp. 703-716, 2023.
Available online at www.jafmonline.net, ISSN 1735-3572, EISSN 1735-3645.
https://doi.org/10.47176/jafm.16.04.1530

Surrogate-Based Design Optimization of a H-Darrieus Wind Turbine Comparing Classical Response Surface, Artificial Neural Networks, and Kriging

D. Cardoso Netto†, R. Ramirez Camacho and N. Manzanares Filho

Federal University of Itajubá, Itajubá, Minas Gerais, 37500-903, Brazil

†*Corresponding Author Email: davidncetto@unifei.edu.br*

(Received August 24, 2022 accepted December 12, 2022)

ABSTRACT

Clean energy sources like wind energy have been receiving much attention, and great emphasis has been given to the design and optimization of horizontal axis wind turbines, but just as important are the vertical axis wind turbines that can be used for generating energy for small businesses, houses, and buildings. This article sought to study the optimal geometrical parameters of a H-Darrieus vertical axis wind turbine using surrogate-based optimization with three different types of surrogate models and compared them. Airfoil chord and thickness were chosen as the design variables and respective ranges set at 0.32-0.6 m and 0.04-0.16 m. All evaluations are carried out for a tip-speed ratio of 1.5. Three different surrogate models were used and compared, namely a quadratic polynomial response surface, an artificial neural network based on radial basis functions called Extreme Learning Machine and a Kriging interpolator. Surrogates were constructed based on an initial sample data distributed according to a full factorial design. A test set was designed to evaluate the accuracy of the surrogates. Both training and testing data sets were generated using 2D CFD modeling to reduce computational cost. From the test set, Extreme Learning Machine surrogate showed the smallest RMSE of 11.24%, followed by Kriging, at 17.64%, and Response Surface of 22.17%. For the optimal designs the same pattern ensued, with optimal power coefficient overestimated by 8.7% for the response surface surrogate, followed by 3.12% and 2.17% for the Kriging interpolator and the Extreme Learning Machine, respectively. Power coefficient curves comparing the three optimal geometries from each surrogate were calculated and plotted. Optimal turbine obtained from Kriging surrogate optimization process resulted in a 7.92% increase in the C_p, whilst Extreme Learning Machine and Response Surface resulted in a 7.86% and 4.29% increase, respectively, all when compared to baseline CFD model. Concluding guidelines are that the quadratic polynomial response surface may not be the best alternative when dealing with complex non-linear relationships as typically present in VAWT simulations. Superior techniques such as Extreme Learning Machine and Kriging could be more suitable for this application.

Keywords: VAWT; Optimization; Surrogate model; Polynomial response surface; Artificial neural networks; Kriging.

NOMENCLATURE

ANN	Artificial Neural Networks	RBF	Radial Basis Function
a	inducing factor	SBO	Surrogate-Based Optimization
A	turbine sweep area	TSR	Tip-Speed Ratio
C_p	power coefficient	U	incoming wind velocity
DOE	Design Of Experiments	VAWT	Vertical Axis Wind Turbine
ELM	extreme learning machine radial basis function artificial neural network	α	angle of attack
		Ω	rotational speed
HAWT	Horizontal Axis Wind Turbine	ϕ	angle between the radius and incoming wind
RSM	Response Surface Method		
RS	Response Surface	θ	VAWT's azimuthal angle
R	turbine radius		

1. INTRODUCTION

The utilization of fossil fuels for energy generation has been growing in the last decades, so has the concern regarding greenhouse gas emissions. Despite its potential for energy production, the burning of fossil fuels results in the emission of gases like CO_2, CH_4, N_2O and vapor of water, that act retaining heat in the atmosphere, thus intensifying the greenhouse effect that is primarily natural.

In Brazil, 3.74 million barrels of oil per day were produced plus 127.4 million of cubic meters of natural gas only in the year of 2020 (ANP 2021). Therefore, the search for and usage of more clean energy sources, such as renewable ones, has been increasing significantly. In terms of wind energy, the world had around 24 GW of installed capacity in 2001 surging to 743 GW in 2020. The Global Wind Energy Council (GWEC) estimates 1000 GW of installed capacity all over the world by the end of 2024 (GWEC 2021).

Wind turbines can be classified according to the position of their rotation axis with respect to the wind. There are horizontal axis wind turbines (HAWT) and vertical axis wind turbines (VAWT). Horizontal axis wind turbines are usually of greater size and used for large-scale energy generation, some have up to 8 MW of generation capacity. On the other hand, vertical axis wind turbines are of a more compact design and have less capacity for energy generation.

Despite having lower energy generation capacity when compared to HAWT, VAWT offer some advantages such as omnidirectional operation, which means they can extract energy of wind coming from either direction, better operation conditions in highly turbulent winds and compact design that makes possible for arrangements with shorter distances between consecutive turbines as investigated by Hansen *et al.* (2021) for example, besides the possibility of installing the turbines in urban areas as means of energy production for houses and small businesses.

Some studies focused on power coefficient, C_p, improvement. Hashem and Mohamed (2017) investigated the effect of different airfoil geometries on C_p and observed that the biggest power coefficient was obtained by a symmetric airfoil. Meana-Fernández *et al.* (2020) proposed a new airfoil shape optimized for VAWT applications. Symmetric and asymmetric airfoils were analyzed. The authors concluded that an asymmetric geometry showed a more suitable aerodynamic behavior for VAWT, with higher lift-to-drag ratio and a delayed stall angle compared to the basis airfoil geometry. Other works used surrogate-based optimization for C_p improvement. The work of Kim *et al.* (2020) focused on the optimization of the blade shape of a H-Darrieus VAWT to attain the maximum power coefficient using the Response Surface Method (RSM). Airfoil maximum thickness and chord length were used as design variables. An overall increase of 12.7% in the power coefficient was observed with the optimal model, compared to the reference model. Elsakka *et al.* (2022) aimed at implementing a response surface optimization (RSO) methodology for a VAWT operating at low wind speed conditions. Solidity, TSR and pitch angle were chosen as design parameters. A Kriging interpolator was implemented for the Response Surface calculation. The optimization process was goal-driven, based on response surface and with the objective of maximizing C_p. DOE and validation of RSO optima were carried out on 2D CFD simulations to reduce computational cost, the authors stated. The authors concluded that RSO combined with CFD simulations of the VAWT provided a powerful tool in the optimal design and for the exploration of the effect of different design parameters on the VAWT performance with reasonable computational costs. Ma *et al.* (2018) aimed to develop an automatic airfoil profile optimization process for improving the power performance of a high solidity VAWT at a moderate TSR. The single objective was to maximize the power coefficient. The power performance of the optimized blade VAWT improved by an average of 18% with respect to the initial airfoil geometry.

Oh (2020) compared the prediction accuracies of different surrogate models constructed using a RSM and Artificial Neural Networks (ANN) for the aerodynamic performance of a wind turbine airfoil. The author used the asymmetric airfoil DU21-A17 as baseline geometry. For the optimization process, a genetic algorithm was used. The optimal airfoil geometry obtained using the ANN surrogate showed a greater lift-to-drag ratio when compared with both baseline and optimal RSM geometry, 18% and 4% increase, respectively. Oh (2020) noted that for datasets with high levels of complexity, the ANN surrogate shows higher accuracy.

Raul and Leifsson (2021) used surrogate-based optimization (SBO) to efficiently find optimum shapes for delaying dynamic stall occurrence over VAWT airfoils. The Kriging method was used as surrogate model and the infill criteria was based on expected improvement. The optimal airfoil shape showed a significant delay in the dynamic stall angle when compared to the baseline airfoil. Hashem and Zhu (2021) applied metamodeling-based parametric optimization to a Savonius-type hydrokinetic turbine inspired by Koi fish. The design parameters were the overlap ratio and the gap ratio. The optimization objective was to maximize C_p at TSR of 1.1. A global metamodel was used to approximate the relationship between the design parameters and the output, namely C_p. RBF neural network metamodel was adopted for its better accuracy with highly nonlinear responses. 2D CFD simulations were applied to estimate the objective in order to reduce the computational cost and time. The optimal design exhibited an increase of 17.6% in the C_p.

Lee and Shin (2020) used a second-order polynomial RS surrogate and observed that the model could reasonably represent the relationship between chord length, twist angle and C_p for a HAWT. Ahmad *et al.* (2022) applied a quadratic RSM surrogate to represent the relationship between chord length, number of blades, pitch angle, distance of blades

from central shaft and rotor height, with C_p for a VAWT and observed R^2 values of 90% and above. Elsakka *et al.* (2022) highlighted that due to the complex non-linear relations between the input parameters and the VAWT performance the Kriging-based surrogate used needed several refinements. Hashem and Zhu (2021) adopted RBF ANN surrogate and emphasized that the approach well represented the design problem.

Cheng and Yao (2022) used and compared a machine learning (ML) method based on ANNs and a RS method to design and optimize a 3D configuration of a U-type Darrieus WT. The machine learning method consisted of a combination of back-propagation neural networks and meta-heuristic algorithms. A quadratic equation model was used for the RS method. The authors observed that the RS method contributed to demonstrating the relationship between design parameters and objective function but also noted that the ML method was superior and fostered more choices for design candidates.

It can be noted that there are several recent works that conducted surrogate-based optimization of VAWTs with different types of surrogate models, but there don't seem to be many comparative studies of the different surrogate methodologies that have been used in the literature. In this context, this paper used surrogate-based optimization to find the optimal geometrical parameters of a VAWT blade airfoil. Three different surrogate models were used and compared, namely a quadratic polynomial response surface, a RBF artificial neural network, called ELM, and a Kriging interpolator. The chosen design parameters were airfoil chord and thickness. The surrogates were constructed and tested through data points evaluated by 2D CFD calculations. The optimum airfoil geometries found by each surrogate were then compared in terms of their lift and drag curves, and their power coefficient curves as function of TSR.

2. THEORETICAL BACKGROUND

2.1 VAWT aerodynamics

Vertical axis wind turbines may have either drag-driven or lift-driven rotors. Lift-driven VAWT are preferred whenever dealing with higher wind speed, thus showing greater power coefficients (Manwell *et al.* 2009). Figure 1 shows one blade of a

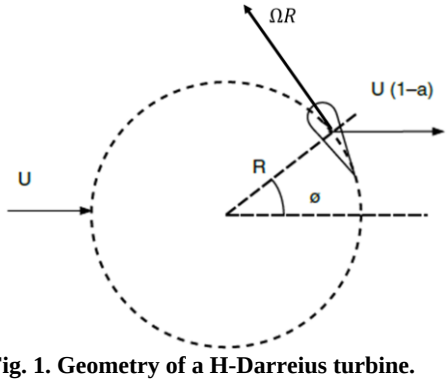

Fig. 1. Geometry of a H-Darreius turbine.

Darrieus wind turbine viewed from above. U represents the incoming wind velocity, R is the turbine radius, Ω is the angular velocity, ϕ is the angle between the radius and the incoming wind and α is the angle of attack. The factor a considers the deceleration effect acting on the wind as it passes through the turbine.

With reference to Fig. 1, two important parameters are defined. The tip-speed ratio is given by Equation 2.1, and the power coefficient is given by Equation 2.2, where P is the power generated by the turbine, A is the VAWT`s frontal area and ρ is the air density.

$$TSR = \frac{\Omega R}{U} \tag{2.1}$$

$$C_P = \frac{P}{\frac{1}{2}\rho A U^3} \tag{2.2}$$

2.2 Governing Equations

Turbulence is characterized by random fluctuations of the flow properties. A way of dealing with these high-frequency fluctuations is by time-averaging the Navier-Stokes equations, resulting in the so-called RANS equations for steady-state and URANS for unsteady simulations. In this process, the flow properties are represented by the sum of the property mean value and its random fluctuations around this mean. Applying this concept to the governing equations such as mass and momentum conservation, the result is a set of equations capable of describing mean flow behavior, represented by Equations 2.3 and 2.4, respectively, for a non-inertial system and assuming incompressible flow.

$$\frac{\partial \bar{W}_i}{\partial x_i} = 0 \tag{2.3}$$

$$\rho\left(\frac{\partial \bar{W}_i}{\partial t} + \bar{W}_j \frac{\partial \bar{W}_i}{\partial x_j} + \vec{a}^*\right) = \rho g_i - \frac{\partial \bar{p}}{\partial x_i} + \frac{\partial}{\partial x_j}\left[\mu\left(\frac{\partial \bar{W}_i}{\partial x_j} + \frac{\partial \bar{W}_j}{\partial x_i}\right) - \rho\overline{W'_i W'_j}\right] \tag{2.4}$$

where ρ, $\bar{p}$, μ and $\bar{W}_i$ are the density, pressure, viscosity, and the components of the relative velocity, respectively. $\vec{a}^*$ is the term containing the sum of tangential, normal and Coriolis accelerations. The terms $-\rho\overline{W'_i W'_j}$ are referred to as the Reynolds stress, assuming the Boussinesq hypothesis, they are given by

$$-\rho\overline{W'_i W'_j} = \mu_T\left(\frac{\partial \bar{W}_i}{\partial x_j} + \frac{\partial \bar{W}_j}{\partial x_i}\right) - \frac{2}{3}\rho k \delta_{ij} \tag{2.5}$$

where μ_T is the turbulent eddy viscosity, k is the turbulent kinetic energy and δ_{ij} is the Kronecker delta function.

The existence of the Reynolds stress gives rise to a problem of closure well known in turbulence modeling. To solve the problem, the Reynolds

stresses need to be modeled. Hence, turbulence models are used. In this work, the standard k-ε model is used. It was proposed initially by Chou (1945), Davidov (1961) and Harlow and Nakayama (1968) and modified after by Jones and Launder (1972) and Launder and Sharma (1974). The model is composed of two transport equations, one for the turbulent kinetic energy k and other for the turbulent dissipation ε (Wilcox 2006).

$$\frac{\partial \rho k}{\partial t} + U_j \frac{\partial \rho k}{\partial x_j} = \tau_{ij} \frac{\partial U_i}{\partial x_j} - \varepsilon + \frac{\partial}{\partial x_j}\left[(\mu + \mu_t/\sigma_k)\frac{\partial k}{\partial x_j}\right] \tag{2.6}$$

$$\frac{\partial \rho \varepsilon}{\partial t} + U_j \frac{\partial \rho \varepsilon}{\partial x_j} = C_{\varepsilon 1} f_1 \frac{\varepsilon}{k} \tau_{ij} \frac{\partial U_i}{\partial x_j} - C_{\varepsilon 2} f_2 \frac{\varepsilon^2}{k} + E + \frac{\partial}{\partial x_j}\left[(\mu + \mu_t/\sigma_\varepsilon)\frac{\partial \varepsilon}{\partial x_j}\right] \tag{2.7}$$

The reader is referred to Jones and Launder (1972) and Launder and Sharma (1974) for the closure coefficients and auxiliary relations.

2.3 Optimization Process: Design of Experiments and Factorial Design

According to Montgomery (2009) the process of planning the experiment is important so that appropriate data will be collected and analyzed, resulting in valid and objective conclusions. The way through which the experiment is planned and conducted is called design of experiments (DOE). Among the existing DOE strategies, the factorial design equally distributes the points across the design space, where each factor is divided in n levels. In the present paper, the optimization was conducted for two factors, corresponding to the design variables, run at four levels each, on what is called a 4^2 factorial design. Figure 2 shows the spatial distribution of such a design.

2.4 Surrogate Model: Classical Polynomial Response Surface

The response surface methodology (RSM) is used for the modeling and analysis of problems where the response of interest is influenced by several independent variables and the objective is to optimize this response. In most RSM problems, the relationship between the response and the variables is unknown (Montgomery 2009). This way, the goal here is to find an approximation for this relationship, be it described by a linear function, or if there is curvature in the system, by higher-order polynomials.

For the optimization process conducted in the current study, a second-order polynomial was chosen as surrogate, shown in Equation 2.8.

$$y = \beta_0 + \sum_{i=1}^{k} \beta_i x_i + \sum_{i=1}^{k} \beta_{ii} x_i^2 + \sum_{i=1}^{k} \sum_{j=i+1}^{k} \beta_{ij} x_i x_j + \epsilon \tag{2.8}$$

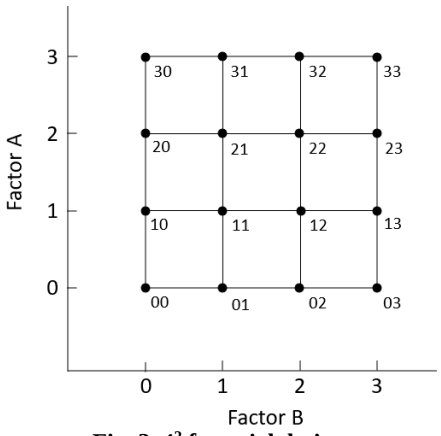

Fig. 2. 4^2 factorial design.

where y is the response of interest, x_i and x_j represent the independent variables, β_i, β_{ii} and β_{ij} are the coefficients to be estimated, k is the number of independent variables and ϵ is the experimental error associated with the approximation.

2.5 Surrogate Model: Radial Basis Function Neural Networks and Extreme Learning Machines

The construction of a radial-basis function (RBF) network involves three layers with their own different roles. First, the input layer is responsible for connecting the network to its environment through what Haykin (1999) calls source nodes. Next, the hidden layer applies a nonlinear transformation from the input space to the hidden layer space, of high dimensionality in most cases. The output layer is the result of a linear combination of the responses from the hidden layer.

The learning process can be said to be equivalent to fitting a surface to the training data in the multidimensional space. And the generalization or prediction calculated by the network is similar to using this fitted multidimensional surface to interpolate the test data, of which the response is unknown.

The nonlinear transformation in the hidden layer is performed through RBFs, shown in Equation 2.9.

$$F(\boldsymbol{x}) = \sum_{i=1}^{N} w_i \varphi(\|\boldsymbol{x} - \boldsymbol{x_i}\|) \tag{2.9}$$

where $\{\varphi(\|\boldsymbol{x} - \boldsymbol{x_i}\|) \mid i = 1, 2, \dots, N\}$ is a set of N arbitrary (generally nonlinear) functions, called radial-basis functions and $\|\cdot\|$ denotes a norm that is usually Euclidean. The known points $\boldsymbol{x}_i$ are taken to be the centers of the radial-basis functions, w_i are the unknown coefficients, also called weights, that can be found through the following set of simultaneous linear equations, by imposing that

$$F(\boldsymbol{x_j}) = d_j \tag{2.10}$$

$$\begin{bmatrix} \varphi_{11} & \varphi_{12} & \cdots & \varphi_{1N} \\ \varphi_{21} & \varphi_{22} & \cdots & \varphi_{2N} \\ \vdots & \vdots & \vdots & \vdots \\ \varphi_{N1} & \varphi_{N2} & \cdots & \varphi_{NN} \end{bmatrix} \begin{bmatrix} w_1 \\ w_2 \\ \vdots \\ w_N \end{bmatrix} = \begin{bmatrix} d_1 \\ d_2 \\ \vdots \\ d_N \end{bmatrix} \tag{2.11}$$

where

$$\varphi_{ji} = \varphi(\|\boldsymbol{x}_j - \boldsymbol{x}_i\|), \quad (j,i) = 1,2,\dots,N \tag{2.12}$$

$$\boldsymbol{d} = [d_1, d_2, \dots, d_N]^T \quad \boldsymbol{w} = [w_1, w_2, \dots, w_N]^T \tag{2.13}$$

The N-by-1 vectors $\boldsymbol{d}$ and $\boldsymbol{w}$ represent the desired response vector and linear weight vector, respectively, where N is the size of the training sample. Equation 2.11 can be rewritten in compact form.

$$\boldsymbol{\Phi w} = \boldsymbol{d} \tag{2.14}$$

Assuming that $\boldsymbol{\Phi}$ is nonsingular and therefore that the inverse matrix $\boldsymbol{\Phi^{-1}}$ exists, Equation 2.14 can be solved, and the weights found.

$$\boldsymbol{w} = \boldsymbol{\Phi^{-1}d} \tag{2.15}$$

Constructing an RBF network usually involves the determination of three parameters. The weights between the input layer and the hidden layer $\boldsymbol{x}_i$ which physically represent the RBF centers, the RBF width μ and the weights between the hidden and output layers, $\boldsymbol{w}_i$. These parameters can be calculated through different learning techniques that depend on how the RBF centers are specified. For the present paper, the learning algorithm called Extreme Learning Machine (ELM) proposed by Huang and Siew (2004) is used. The radial-basis function used in the ELM is the Gaussian given by Equation 2.16.

$$G(\boldsymbol{x}_i, \mu, \boldsymbol{x}) = \exp\left(-\frac{1}{\mu}\|\boldsymbol{x} - \boldsymbol{x}_i\|^2\right), \quad i = 1,2,\dots,N \tag{2.16}$$

ELM centers are chosen randomly from the training data and RBF width is determined through a sensitivity analysis. This way, the only parameter left to be determined are the weights $\boldsymbol{w}_i$, that can be calculated through Equation 2.15. In order to avoid problems with the matrix inversion $\boldsymbol{\Phi^{-1}}$, Huang and Siew (2004) suggest the use of the pseudoinverse by singular value decomposition (SVD).

Once the weights are determined, RBF network predictions can be found by calculating the $\boldsymbol{G}$ matrix for the desired set of points and multiplying it by the already calculated weights $\boldsymbol{w}$.

$$\boldsymbol{Y}_{pred} = \boldsymbol{Gw} \tag{2.17}$$

where the G_{ij}-th element of $\boldsymbol{G}$ corresponds to the value of the Gaussian function centered at $\boldsymbol{x}_i$ and evaluated at $\boldsymbol{x}_j$.

2.6 Surrogate Model: Kriging

Following Jones' (2001) approach to the derivation of Kriging equations, suppose one wants to make a prediction for the value of a function $y(\boldsymbol{x})$ at a point $\boldsymbol{x}$ in the domain. Before the function can be evaluated at some points in the domain, one assumes an uncertainty associated with this estimation that can be represented by the random variable $Y(\boldsymbol{x})$ and which value may vary inside the range of a normal distribution of mean μ and variance σ^2.

If two points $\boldsymbol{x}_i$ and $\boldsymbol{x}_j$ are taken, there will also be an uncertainty associated with the function values at these points. However, assuming the function is continuous, it is expected that the function values $y(\boldsymbol{x}_i)$ and $y(\boldsymbol{x}_j)$ will tend to be close as the distance $\|\boldsymbol{x}_i - \boldsymbol{x}_j\|$ decreases. Statistically speaking, the random variables $Y(\boldsymbol{x}_i)$ and $Y(\boldsymbol{x}_j)$ will be highly correlated if $\|\boldsymbol{x}_i - \boldsymbol{x}_j\|$ is small. Such correlation is given by

$$corr[Y(\boldsymbol{x}_i), Y(\boldsymbol{x}_j)] = \exp\left(-\sum_{l=1}^{d} \theta_l |x_{il} - x_{jl}|^{p_l}\right) \tag{2.18}$$

It can be noted that if $\boldsymbol{x}_i = \boldsymbol{x}_j$ the correlation is 1, and as $\|\boldsymbol{x}_i - \boldsymbol{x}_j\| \to \infty$ the correlation tends to zero. The hyperparameter θ_l determines how fast the correlation decays as one moves in the l coordinate direction. For example, higher values of θ_l are useful in modeling functions that change value rapidly over small variations in l. The p_l parameter determines the smoothness of the function.

The uncertainty associated with the function values for n points can be represented by the random vector $\boldsymbol{Y}$ whose mean is equal to $\boldsymbol{1}\mu$, where $\boldsymbol{1}$ is a $n \times 1$ vector of ones and covariance matrix given by Equation 2.20.

$$\boldsymbol{Y} = \begin{pmatrix} Y(\boldsymbol{x}_1) \\ \vdots \\ Y(\boldsymbol{x}_n) \end{pmatrix} \tag{2.19}$$

$$Cov(\boldsymbol{Y}, \boldsymbol{Y}) = \sigma^2 \boldsymbol{\Psi} \tag{2.20}$$

where $\boldsymbol{\Psi}$ is a $n \times n$ correlation matrix with (i,j) elements equal to

$$\boldsymbol{\Psi} = \begin{pmatrix} corr[Y(\boldsymbol{x}_1), Y(\boldsymbol{x}_1)] & \cdots & corr[Y(\boldsymbol{x}_1), Y(\boldsymbol{x}_n)] \\ \vdots & \ddots & \vdots \\ corr[Y(\boldsymbol{x}_n), Y(\boldsymbol{x}_1)] & \dots & corr[Y(\boldsymbol{x}_n), Y(\boldsymbol{x}_n)] \end{pmatrix} \tag{2.21}$$

The distribution of $\boldsymbol{Y}$ depends upon the parameters μ, σ^2, θ_l and p_l that are estimated as to maximize the likelihood L of the observed function values $\boldsymbol{y}$, which means that the model of the function's typical behavior is being most consistent with the data observed.

The Kriging prediction $\hat{y}(\boldsymbol{x}^*)$ at an unknown point $\boldsymbol{x}^*$ is given by

$$\hat{y}(\boldsymbol{x}^*) = \hat{\mu} + \boldsymbol{\psi}^T \boldsymbol{\Psi}^{-1}(\boldsymbol{y} - \mathbf{1}\hat{\mu}) \tag{2.22}$$

where

$$\hat{\mu} = \frac{\mathbf{1}^T \boldsymbol{\Psi}^{-1} \boldsymbol{y}}{\mathbf{1}^T \boldsymbol{\Psi}^{-1} \mathbf{1}} \tag{2.23}$$

$$\boldsymbol{\psi} = \begin{pmatrix} corr[Y(\boldsymbol{x}^*), Y(\boldsymbol{x_1})] \\ \vdots \\ corr[Y(\boldsymbol{x}^*), Y(\boldsymbol{x}_n)] \end{pmatrix} = \begin{pmatrix} \psi_1 \\ \vdots \\ \psi_n \end{pmatrix} \tag{2.24}$$

3. METODOLOGY

The analyses are conducted in two dimensions due to the need to contain the computational cost, and Bianchini *et al.* (2017) concluded that 2D VAWT simulations can give acceptable results with reasonable mesh, timestep and geometry settings. and assuming incompressible flow. Finite volume method is used. The VAWT geometry used is based on the work of Bravo *et al.* (2007) that conducted an experimental study for a 3-bladed H-Darreius wind turbine in wind tunnel.

The mesh was generated using ANSYS® ICEM CFD. ANSYS® FLUENT was used for flow solution and the optimization process was conducted in modeFRONTIER® that allows for integration of third-party software in a single workflow. The NSGA-II optimization algorithm was used. Response surface functions were derived using Minitab®.

3.1 Geometry

When simulating a VAWT rotor, the first step is defining the domain which contains the rotor. The dimensions of the domain should be defined in ways that the fluid properties at the boundaries are close to that of the free stream. The domain was divided into three subdomains in order to favor the optimization process. Figure 3 shows the subdomain called *farfield* encompassing the other two subdomains shown in detail at Fig. 4 a) and b). Subdomains 2 and 3 are noninertial, and subdomain 3 is the only geometry that changes in the optimization process, saving computational time.

The turbine analyzed in Bravo *et al.* (2007) work had a rotor with 2.5 m diameter, 3 m height and the symmetric NACA0015 as blade airfoil, with a 0.4 m chord and a 0.06 m maximum effective thickness. The geometry generated had specified dimensions except for the height, as the analysis was conducted in two dimensions. Domain dimensions were chosen based on the work of Rezaeiha *et al.* (2017) that studied guidelines for minimum domain size for CFD simulation of VAWTs. The authors concluded that 10 and 25 times the rotor diameter for the inlet and outlet, respectively, and 1.5 times the rotor diameter for the rotating subdomain were enough to prevent overestimating the turbine performance.

3.2 Computational grid and grid independence

Variations in mesh size can significantly alter the CFD output up to a point, when subsequent mesh refinements lead to small changes in the desired output. At this point, the results are said to be grid independent.

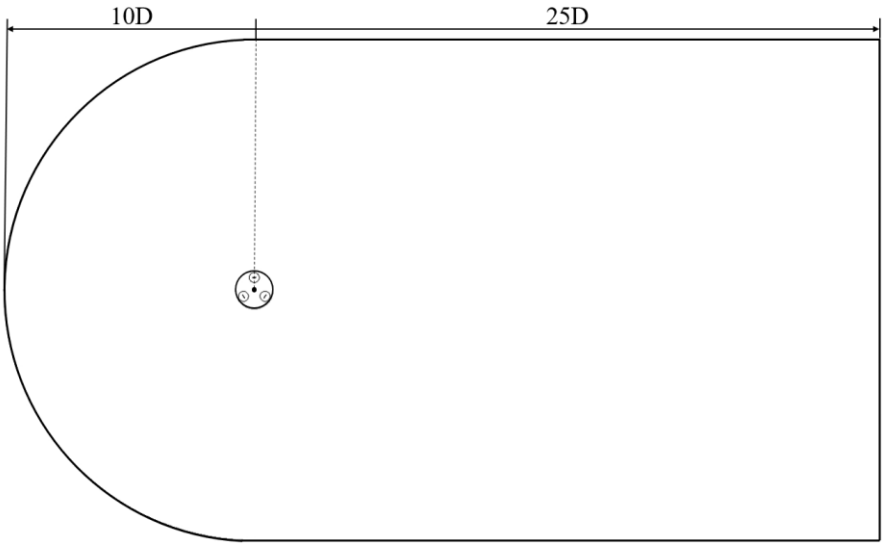

Fig. 3. Subdomain 1, *farfield*.

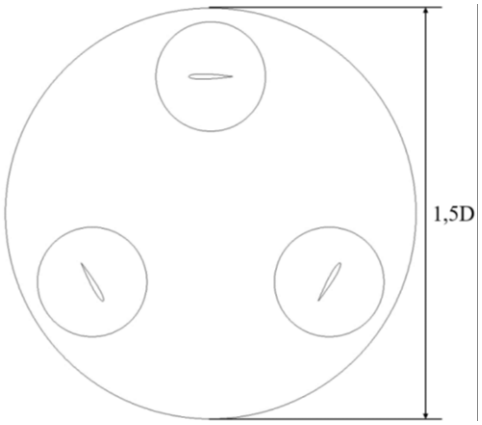

(a) Subdomain 2, *rotor*

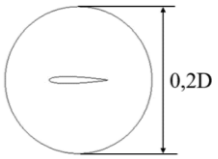

(b) Subdomain 3, *VAWT blades*

Fig. 4. Noninertial subdomains

The first step at a grid independence study is to generate a baseline mesh and set the flow conditions for the CFD solver. These conditions are kept the same for all the grid configurations. A turbulence model comparison study was carried out between the k-ε standard and k-ω SST models for the current problem. It was shown that, despite the latter being more widely used in literature, it also required a more refined mesh and took twice the time compared to the k-ε model. Therefore, a good compromise between

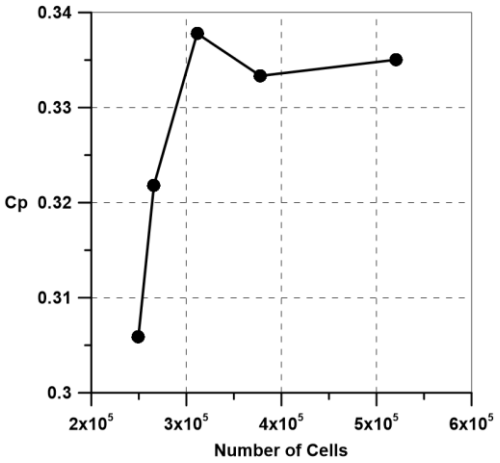

Fig. 5. Results of grid independence study as a function of power coefficient.

accuracy and computational cost could be gained using the k-ε standard model (Pan *et al.* 2020; Jang *et al.* 2021; Ahmad *et al.* 2022), which was adopted for the subsequent CFD simulations.

Using the baseline geometry with NACA0015, simulation conditions were set at 10 m/s velocity at the inlet with a 5% turbulence intensity. The noninertial subdomains were treated as moving reference frame. Results of the grid independence study are shown in Fig. 5.

Despite the difference in C_p from the 377,883-cell mesh and the 520,683-cell mesh being less than 1%, the latter was chosen since the objective of the CFD simulations was first to generate the training data for the surrogates. Once built, the surrogates are used in the optimization process, so, even though the

computational time in this step was greater with the 520,683-cell mesh, it was way less than would be allowable if the optimization process was conducted with the CFD solver instead of the surrogates.

Figure 6 shows the chosen mesh and the smooth transition between the interfaces of the subdomains.

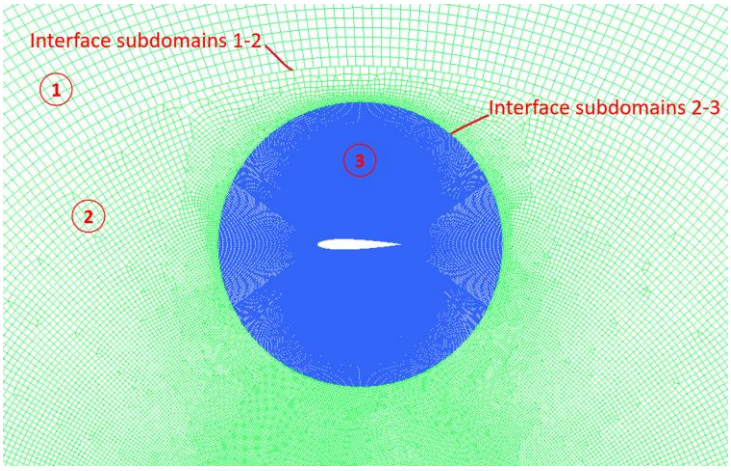

Fig. 6. Detail of mesh around one blade and mesh interfaces.

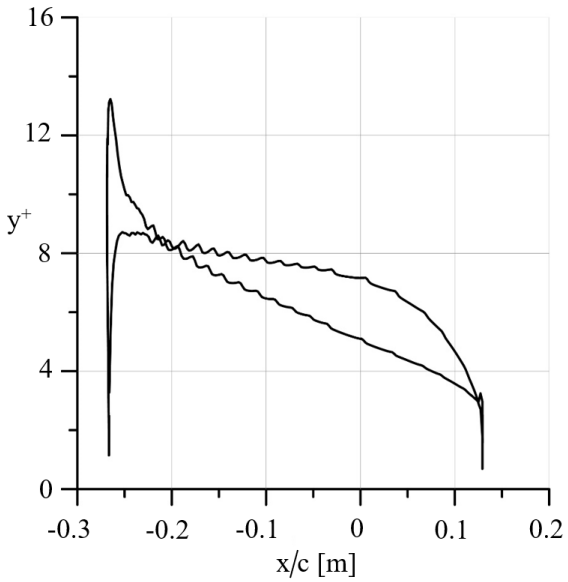

Fig. 7. y^+ distribution over the airfoil surface, in terms of normalized x coordinate.

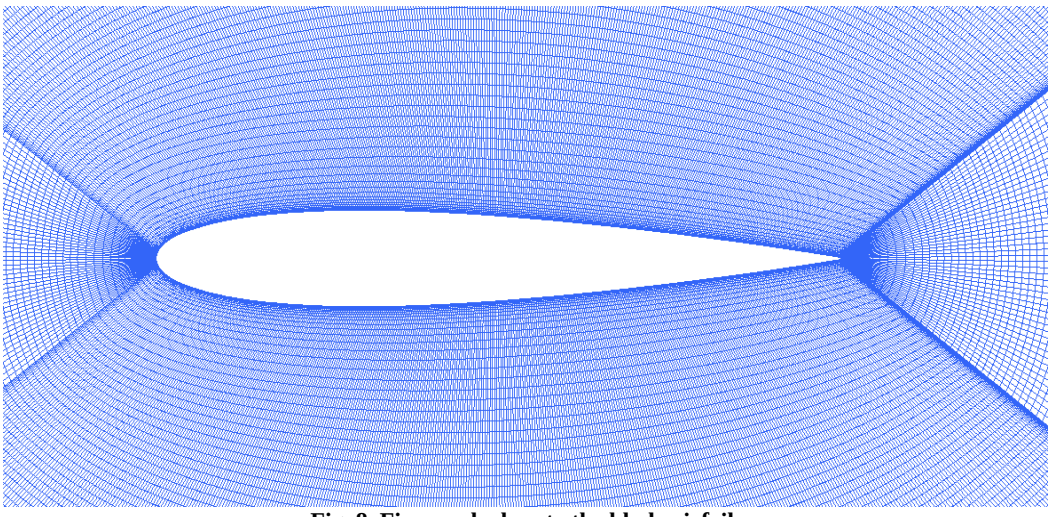

Fig. 8. Fine mesh close to the blade airfoil.

Closer to the airfoil surface, the mesh refinement was enough to assure a maximum y^+ of 14 as the standard k-ε turbulence model uses wall functions to model the boundary layer. Figure 7 shows y^+ as a function of the airfoil x coordinate, normalized in terms of the airfoil chord, c. Figure 8 shows the mesh near the blade airfoil.

3.3 Boundary and initial conditions

The inlet (represented by 1 at Fig. 9) was set as velocity-inlet and the x-component of velocity set as 10m/s. Pressure-outlet condition was attributed to the outlet with a 0 Pa gauge pressure. Region 3 is composed of airfoil walls, hence stationary and no-slip wall conditions were set.

Besides the usual boundary conditions, as the domain is divided into three subdomains and two of them are noninertial, it is necessary that two more boundary conditions are specified. First, the faces that delimit each subdomain and are in contact with the subjacent subdomain create an interface, which are shown by 4 in Fig. 9. Thus, interface condition was set to assure that the information is transmitted through adjacent cells. Lastly, the noninertial core shown by 5 was set as mesh motion with angular velocity of 12 rad/s, this way both the mesh and its reference frame are rotated. The combination of a wind velocity of 10 m/s and an angular velocity of 12 rad/s results in a TSR equal to 1.5. SIMPLE method was used for pressure-velocity coupling. Step time size was set at 0.005 s for a total of 630 step times, that is, 3.15 s of flow time was calculated, corresponding to approximately 6 cycles.

3.4 Surrogate-based optimization process

For the optimization process, airfoil chord and thickness were chosen as design variables (factors)

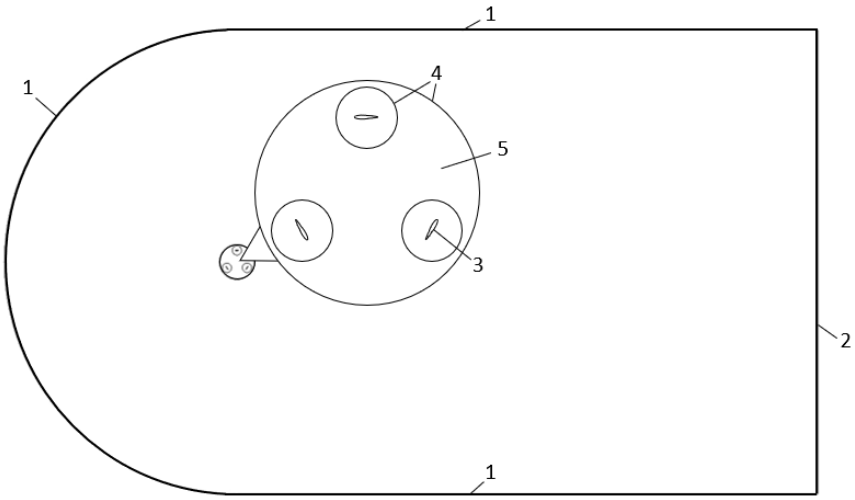

Fig. 9. Faces and regions for boundary condition specification.

and respective ranges set at 0.32-0.6 m and 0.04-0.16 m. The turbine power coefficient was the response of interest, which was maximized for a TSR of 1.5, close to the peak Cp observed by Bravo *et al.* (2007) at TSR equal to 1.6.

Using modeFRONTIER® for the factorial DOE, the design space was divided into 4 levels for each factor and the power coefficient was obtained by CFD calculations for each of the 16 design combinations. The results obtained in this process were used as training data set for the construction of the surrogates. Figure 10 exhibits the surrogate-based optimization flowchart. The power coefficient was obtained through a filtering process. At the first stages of operation, the VAWT shows an instable behavior for moment coefficient, and these values must not be taken for the analysis. This way, the moment and power coefficients were averaged starting at 2 cycles and over to 6 cycles.

3.5 Construction and Testing of the Surrogate Models

After the training data was generated, the surrogate models were constructed based on the sample points represented in Fig. 11. The models were, then, validated against nine set of points, located at the middle distance from the DOE points, as also shown in Fig. 11. Table 1 shows the points and the RMSE associated with each surrogate prediction.

The RS surrogate showed the higher RMSE, which was expected, since the real function behavior is unlikely to be as smooth as a second-order polynomial surface. RBF and Kriging surrogates RMSE were of 11.24% and 17.64%, respectively. From that, it can be said that the RBF surrogate had the highest accuracy for the proposed process.

In section 4 are discussed the results of the CFD model validation and the results of the optimization process, e.g., the optimal airfoil geometries, their lift and drag curves and the power coefficient curves as function of TSR.

4. RESULTS AND DISCUSSION

4.1 CFD Model Validation

The power coefficient obtained by the grid independent CFD model was compared against the

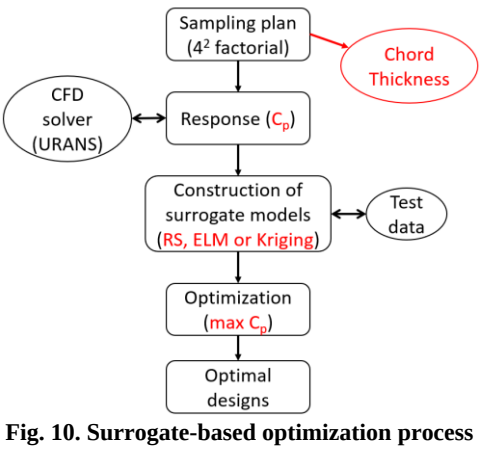

Fig. 10. Surrogate-based optimization process flowchart.

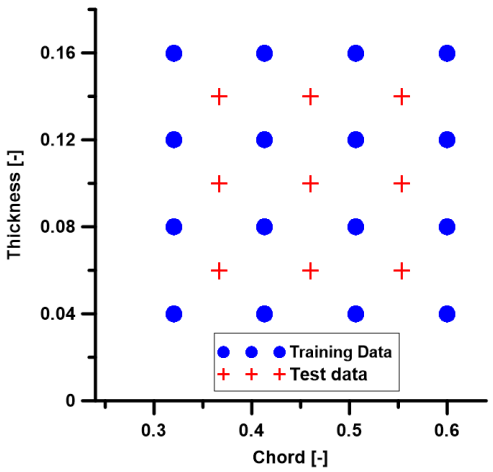

Fig. 11. Training and test data sets.

Table 1 Surrogate RMSE at test data.

Test Data			RS prediction	Error [%]	RBF prediction	Error [%]	Kriging prediction	Error [%]
Chord	Thickness	C_p						
0.367	0.060	0.420	0.366	14.91%	0.398	5.59%	0.385	9.21%
0.367	0.100	0.438	0.411	6.71%	0.449	2.39%	0.452	3.04%
0.367	0.140	0.360	0.330	8.92%	0.340	5.77%	0.324	10.83%
0.460	0.060	0.415	0.411	1.08%	0.409	1.56%	0.400	3.72%
0.460	0.100	0.468	0.487	3.89%	0.483	3.11%	0.486	3.76%
0.460	0.140	0.450	0.437	2.91%	0.441	1.95%	0.442	1.94%
0.553	0.060	0.386	0.372	3.65%	0.369	4.68%	0.362	6.71%
0.553	0.100	0.438	0.480	8.70%	0.440	0.53%	0.443	1.20%
0.553	0.140	0.436	0.461	5.52%	0.418	4.23%	0.416	4.62%
			MSE	4.91%	**MSE**	1.26%	**MSE**	3.11%
			RMSE	**22.17%**	**RMSE**	**11.24%**	**RMSE**	**17.64%**

experimental data of Bravo *et al.* (2007). First, it is worth noting the differences between both configurations. The CFD model was based on a two-dimensional configuration and the domain boundaries were set so as not to interfere in the flow properties. Whilst, the work of Bravo *et al.* (2007) was conducted on a 9x9 m² low speed wind tunnel. Figure 12 compares the power coefficient curves from both settings as a function of TSR. For lower values of TSR, ranging from 0.5 to 1.1, a reasonable accordance can be observed. As the wind velocity increases and, therefore TSR, the power coefficient from the CFD model grows at a bigger rate than the one observed on experiments, but still showing a qualitative agreement with experimental data, with a peak Cp of 0.473 at a TSR of 1.8 for the CFD model versus 0.296 for a TSR of 1.6 from experimental data. The CFD model overpredicts the power coefficient for TSR greater than 1.2.

The differences observed from Fig. 12 may be related to the differences in the settings. A two-dimensional model tends to simplify the tridimensional structures that are characteristic of turbulent flows and does not consider the dissipative tridimensional vortices that are formed at the edges of the blades. As the works of Gosselin *et al.* (2016) and Elsakka *et al.* (2022) concluded, the lower the turbine's aspect ratio, the higher the tendency of the 2D simulations to overpredict the C_p, with up to 41% of overprediction observed by Elsakka *et al.* (2022) for a turbine with aspect ratio equal to 1, close to the current turbine's aspect ratio of 1.2. Corroborating to that is the fact that the difference in C_p increases as the wind velocity increases and the flow becomes even more turbulent. Nonetheless, considering that the surrogate models were all constructed from data obtained with the same CFD model, for the sake of comparing the surrogates, the CFD model can be considered suitable.

4.2 Optimal designs

Once the accuracy of the surrogate models is calculated, they are passed on to the optimization process to find an optimal airfoil design for the problem. The search algorithm used is the NSGA-II. Each evaluation of the surrogates takes no more than 15s, and the process converges to the optimum after around a hundred individuals. Figure 13 shows the convergence history of the optimization process using the Kriging surrogate.

Table 2 shows the optimal values of chord, thickness, the proportion of thickness over chord and respective power coefficients, either the C_p predicted by the surrogates and the ones evaluated using CFD, for each surrogate with the baseline for comparison. From Table 2, it is worth noting that the accuracy of the surrogate predictions for the optimal designs followed the same pattern from the test data validation on section 3.5, with the quadratic polynomial RS prediction overestimating the C_p by 8.7%, followed by the Kriging interpolator and the ELM with 3.12% and 2.17%, respectively. Besides, if one were to be guided in the optimization process solely from the surrogate predictions, the quadratic polynomial RS surrogate would have led to an optimal point that, as the CFD evaluation showed, turned out not to be optimal when compared to the other surrogates.

Figure 14 compares the optimal airfoil geometries obtained through each optimization process and the

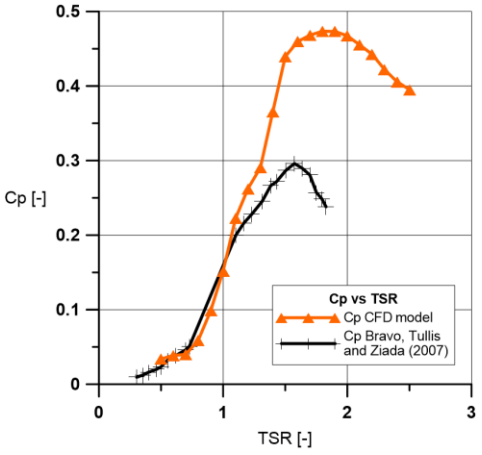

Fig. 12. Comparison of power coefficient from CFD model and experimental data.

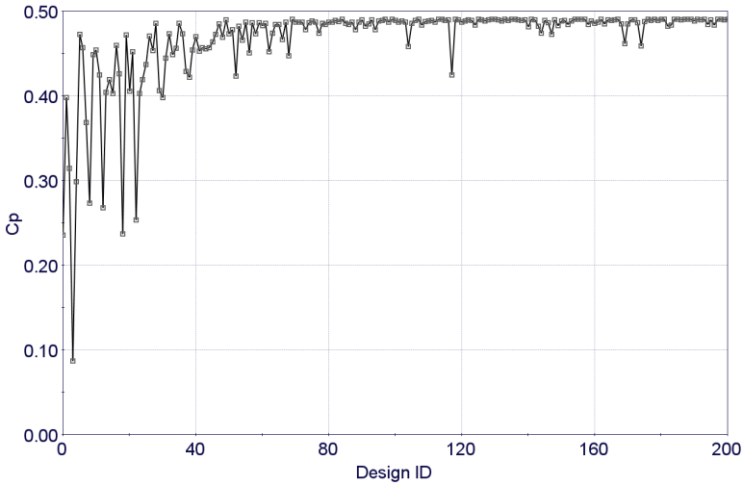

Fig. 13. Convergence history for optimization process with Kriging surrogate.

Table 2 Optimal values and power coefficients.

Optimal geometries.					
Surrogate	**Chord**	**Thickness**	**Thickness/Chord proportion**	**C_p (surrogate)**	**C_p (CFD)**
Baseline	0.4000	0.1600	0.4000	-	0.4395
Classical RS	0.5072	0.1086	0.2142	0.4982	0.4583
ELM	0.4367	0.0953	0.2183	0.4842	0.4739
Kriging	0.4353	0.0962	0.2209	0.4891	0.4743

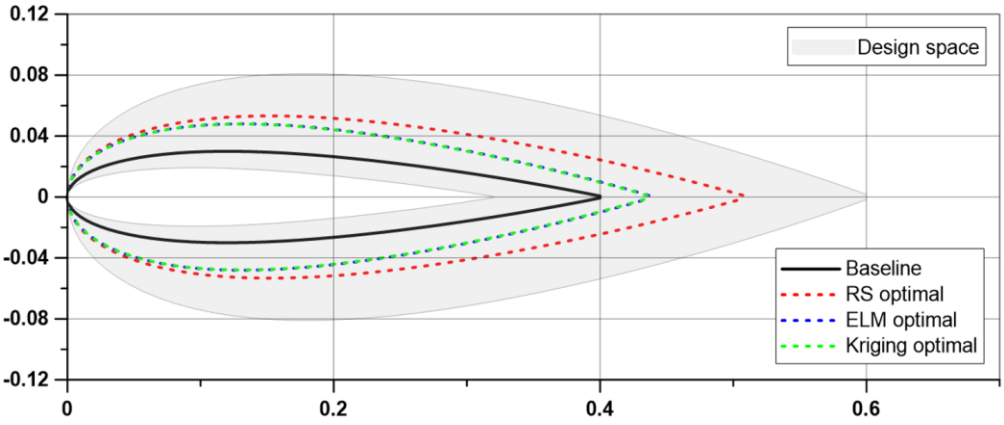

Fig. 14. Optimal airfoil geometries and baseline airfoil.

baseline airfoil. Lengths are scaled with reference to the baseline chord. It can be noted that the response surface optimization led to a bigger airfoil overall, with greater thickness and chord. Both surrogates ELM and Kriging resulted in very similar geometries. The tendency of the optimization processes was to increase the airfoil thickness and chord with respect to the baseline geometry.

Figures 15 and 16 exhibit the drag and lift coefficient curves, respectively, of a single blade airfoil over an entire revolution at TSR of 1.5. From the drag coefficient curve, it can be seen that the RS optimal airfoil's drag is the highest within azimuth angle θ from 30° to 120°, with its peak at 90° (airfoil chord is perpendicular to the incoming wind in upwind region). Since it is the thickest and longest of all airfoils, this was expected. An important effect can be noted, all the optimal airfoils showed reduced drag compared to the baseline within 210° and 330°. Furthermore, the lift coefficient curves exhibit similar behavior with reduced lift for the optimal geometries within 210° and 330°, besides a lower peak within 120° and 150°.

With the optimal geometries in hand, the power coefficient curves were calculated and compared by plotting against one another, as shown in Fig. 17. As

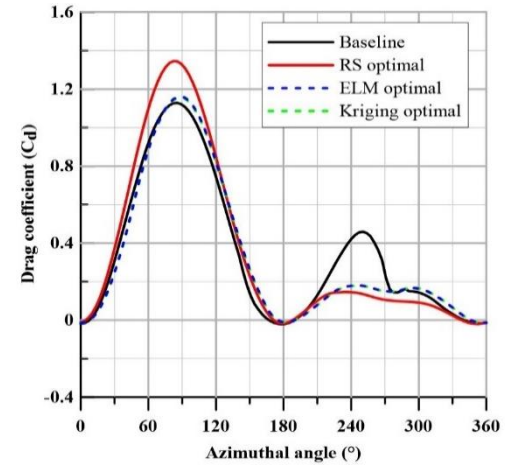

Fig. 15. Drag coefficient for the baseline and optimal geometries. Re = 1.71x10^6.

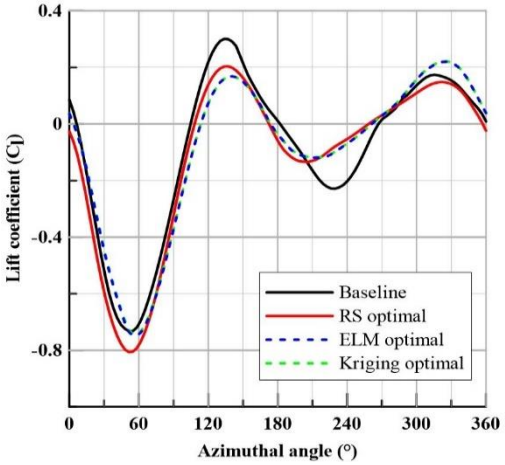

Fig. 16. Lift coefficient for the baseline and optimal geometries. Re = 1.71x10^6.

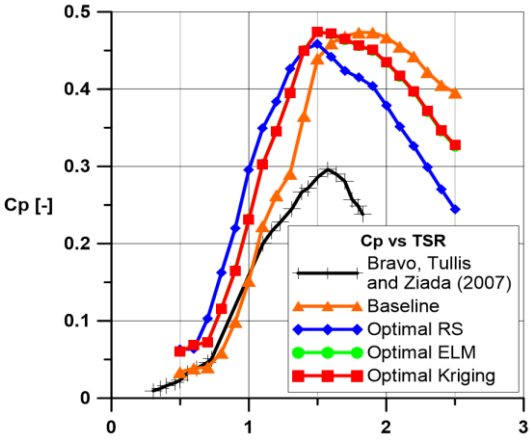

Fig. 17. C_p versus TSR for optimal and baseline designs and experimental data from Bravo *et al.* (2007).

can be seen, all the optimal geometries resulted in greater C_p when compared to the baseline CFD model for TSR ranging from 0.5 up to 1.5 for the RS optimal, and 1.7 for the other two surrogates, ELM, and Kriging. At the optimization point of TSR equal to 1.5, the optimal surrogate designs showed a C_p of 0.458 for the RS, 0.473 for the ELM and 0.474 for the Kriging surrogate, an increase of 4.29%, 7.86% and 7.92% respectively, with respect to the baseline CFD model C_p of 0.439. As the optimal airfoil geometry found by the ELM and Kriging surrogates were very close, it was expected that the power coefficient curve would be as well. It is interesting to note that the RS optimal resulted in higher values of C_p for TSR between 0.5-1.4 when compared to the ELM and Kriging optimal designs. After TSR of 1.4, this behavior is reversed, with the RS optimal showing lower values of C_p than those of ELM and Kriging.

5. CONCLUSIONS

In this work, a surrogate-based optimization process was conducted with the goal of maximizing the power coefficient of a H-Darrieus VAWT. Chord and thickness were chosen as design variables. A quadratic polynomial response surface, extreme learning machine and a Kriging interpolator were used as surrogates and compared. The surrogates were constructed based on a training data distributed throughout the design space by a factorial DOE. Power coefficient was obtained through a grid independent CFD model.

The surrogates constructed showed reasonable accuracy when checked against the test data set with the largest RMSE being that of the RS, followed by Kriging and ELM. The optimization process conducted using the surrogates was significantly faster than it would be using only the CFD model, due to the substantial difference in computational time, and converged after a couple hundred individuals. RS surrogate optimization resulted in an airfoil geometry with greater dimensions overall. ELM and Kriging surrogates resulted in very similar airfoil geometries, with thickness and chord smaller than that of the RS optimal airfoil.

Comparing the optimal designs found by the three different surrogates and their respective C_p predictions, it was observed that even though the RS surrogate predicted an optimal design with greater C_p than that from the ELM and Kriging surrogates, it was not the case once the CFD evaluations were carried out for the designs. This way, one would be advised that the quadratic polynomial RS surrogate methodology may not be the best alternative when dealing with complex non-linear input-output relationships as is generally the case for VAWT simulations and that superior techniques such as ELM and Kriging could be more suitable for this application.

From the lift and drag curves it could be seen that…

Power coefficient curves revealed that the thicker airfoil found at the RS surrogate optimization produced slightly more power at lower TSR and, thus, lower wind velocities, whilst the airfoils from ELM and Kriging surrogate optimization, despite having similar aspect ratios with respect to the RS

airfoil, better produced power at higher wind velocities.

Future work will focus on robust/multipoint optimization for VAWT using a range of TSR rather than a single point. This way, the resulting optimal turbine could have greater values of power coefficient over a range of velocities of operation, since real wind conditions tend to vary.

REFERENCES

Ahmad, M., A. Shahzad, F. Akram, F. Ahmad and S. I. A. Shah (2022). Design optimization of Double-Darrieus hybrid vertical axis wind turbine. *Ocean Engineering* 254, 111171.

ANP, Oil and NGL National Production in cubic meters. Available at: <https://www.gov.br/anp/pt-br/canais_atendimento/imprensa/noticias-comunicados/producao-de-petroleo-e-gas-teve-recorde-em-2020-e-aumentou-52-71-em-relacao-a-2010>. Access on: January 14th, 2022.

Bianchini, A., F. Balduzzi, P. Bachant, G. Ferrara and L. Ferrari (2017). Effectiveness of two-dimensional CFD simulations for Darrieus VAWTs: a combined numerical and experimental assessment. *Energy Conversion and Management* 136, 318-328.

Bravo, R., S. Tullis and S. Ziada (2007). Performance testing of a small vertical-axis wind turbine. In *Proceedings of the 21st Canadian Congress of Applied Mechanics*, Mechanical Engineering Department, McMaster University, Canada.

Cheng, B. and Y. Yao (2022). Design and optimization of a novel U-type vertical axis wind turbine with response surface and machine learning methodology. *Energy Conversion and Management* 273, 116409.

Chou, P. Y. (1945). On the velocity correlations and the solution of the equations of turbulent fluctuation. *Quarterly of Applied Mathematics* 3(1), 38-54.

Davidov, B. I. (1961). *on the Statistical Dynamics of an Incompressible Fluid.* Doklady Akademiya Nauk SSSR 136, 47.

Elsakka, M. M., D. B. Ingham, L. Ma, M. Pourkashanian, G. H. Moustafa and Y. Elhenawy (2022). Response surface optimisation of vertical axis wind turbine at low wind speeds. *Energy Reports* 8, 10868-10880.

Gosselin, R., G. Dumas and M. Boudreau (2016). Parametric study of H-Darrieus vertical-axis wind turbines using CFD simulations. *Journal of Renewable and Sustainable Energy* 8(5), 053301.

GWEC, *Global Wind Report 2021*. Available at: <https://gwec.net/global-wind-report-2021/>. Access on: January 14th, 2022.

Hansen, J. T., M. Mahak and I. Tzanakis (2021). Numerical modelling and optimization of vertical axis wind turbine pairs: A scale up approach. *Renewable Energy* 171, 1371-1381.

Harlow, F. H. and P. I. Nakayama (1968). *Transport of Turbulence Energy Decay Rate.* Alamos Science Lab, University of California Report.

Hashem, I. and M. H. Mohamed (2017). Aerodynamic performance enhancements of H-rotor Darrieus wind turbine. *Energy* 142, 531-545.

Hashem, I. and B. Zhu (2021). Metamodeling-based parametric optimization of a bio-inspired Savonius-type hydrokinetic turbine. *Renewable Energy* 180, 560-576.

Haykin, S. (1999). *Neural Networks a comprehensive foundation. McMaster University.* Pearson Education.

Huang, G. and C. K. Siew (2004) Extreme Learning Machine: a new scheme of feedforward neural networks. *IEEE International Joint Conference on Neural Networks* 2, 985-990.

Jang, H., Y. Hwang, I. Paek and S. Lim (2021). Performance evaluation and validation of h-darrieus small vertical axis wind turbine. *International Journal of Precision Engineering and Manufacturing-Green Technology* 8, 1687-1697.

Jones, D. R. (2001). A taxonomy of global optimization methods based on response surfaces. *Journal of Global Optimization* 21, 345-383.

Jones, W. P. and B. E. Launder (1972). The prediction of laminarization with a two-equation model of turbulence. *International Journal of Heat and Mass Transfer* 15, 301-314.

Kim, C. K., S. Ali, S. M. Lee and C. M. Jang (2020). Blade optimization of a small vertical-axis wind turbine using the response surface method. *Renewable Energy and Sustainable Buildings* 801-812.

Launder, B. E. and B. I. Sharma (1974). Application of energy dissipation model of turbulence to the calculation of flow near a spinning disc. *Letters in Heat and Mass Transfer* 1(2), 131-137.

Lee, S. L. and S. Shin (2020). Wind turbine blade optimal design considering multi-parameters and response surface method. *Energies* 13(7).

Ma, N., H. Lei, Z. Han, D. Zhou, Y. Bao, K. Zhang, L. Zhou and C. Chen (2018). Airfoil optimization to improve power performance of a high-solidity vertical axis wind turbine at a moderate tip speed ratio. *Energy* 150, 236-252.

Manwell, J. F., J. G. McGowan and A. L. Rogers (2009) *Wind Energy Explained, Theory, Design and Application.* Wiley.

Meana-Fernández, A., L. Díaz-Artos, J. M. Fernández Oro and S. Velardez-Suárez (2020). An optimized airfoil geometry for vertical-axis wind turbine applications. *International Journal of Green Energy* 17, 181-195.

Montgomery, D. G. (2009). *Design and Analysis of Experiments. Arizona State University*. John Wiley & Sons, Inc. Ninth edition.

Oh, S. (2020). Comparison of a response surface method and artificial neural network in predicting the aerodynamic performance of a wind turbine airfoil and its optimization. *Applied Sciences* 10(18), 6277.

Pan, L., H. Xiao, Y. Zhang and Z. Shi (2020). Research on aerodynamic performance of j-type blade vertical axis wind turbine. In *Chinese Control and Decision Conference*, IEEE.

Raul, V. and L. Leifsson (2021). Surrogate-based aerodynamic shape optimization for delaying airfoil dynamic stall using Kriging regression and infill criteria. *Aerospace Science and Technology* 111, 106555.

Rezaeiha, A., I. Kalkman and B. Blocken (2017). CFD simulation of a vertical axis wind turbine operating at a moderate tip speed ratio: Guidelines for minimum domain size and azimuthal increment. *Renewable Energy* 107, 373-385.

Wilcox, D. C. (2006). *Turbulence Modeling for CFD*. DCW Industries, Inc., La Canada, CA.